nature materials

ARTICLES

PUBLISHED ONLINE: 26 AUGUST 2012 | DOI: 10.1038/NMAT3404

Macroporous nanowire nanoelectronic scaffolds for synthetic tissues

Bozhi Tian[1,2,3†], Jia Liu[1†], Tal Dvir[2,4†], Lihua Jin[5], Jonathan H. Tsui[2], Quan Qing[1], Zhigang Suo[5], Robert Langer[3,4], Daniel S. Kohane[2*] and Charles M. Lieber[1,5*]

The development of three-dimensional (3D) synthetic biomaterials as structural and bioactive scaffolds is central to fields ranging from cellular biophysics to regenerative medicine. As of yet, these scaffolds cannot electrically probe the physicochemical and biological microenvironments throughout their 3D and macroporous interior, although this capability could have a marked impact in both electronics and biomaterials. Here, we address this challenge using macroporous, flexible and free-standing nanowire nanoelectronic scaffolds (nanoES), and their hybrids with synthetic or natural biomaterials. 3D macroporous nanoES mimic the structure of natural tissue scaffolds, and they were formed by self-organization of coplanar reticular networks with built-in strain and by manipulation of 2D mesh matrices. NanoES exhibited robust electronic properties and have been used alone or combined with other biomaterials as biocompatible extracellular scaffolds for 3D culture of neurons, cardiomyocytes and smooth muscle cells. Furthermore, we show the integrated sensory capability of the nanoES by real-time monitoring of the local electrical activity within 3D nanoES/cardiomyocyte constructs, the response of 3D-nanoES-based neural and cardiac tissue models to drugs, and distinct pH changes inside and outside tubular vascular smooth muscle constructs.

The design and functionalization of porous materials have been actively pursued to enable new material properties and applications[1–3]. In particular, the development of synthetic 3D macroporous biomaterials as extracellular matrices (ECMs) represents a key area because functionalized 3D biomaterials allow for studies of cell/tissue development in the presence of spatiotemporal biochemical stimulants[3–6], and the understanding of the pharmacological response of cells within synthetic tissues is expected to provide a more robust link to *in vivo* disease treatment than that from 2D cell cultures[6–8]. Advancing further such biomaterials requires capabilities for monitoring cells throughout the 3D micro-environment[6]. Although electrical sensors are attractive tools, it has not been possible to integrate such elements with porous 3D scaffolds for localized real-time monitoring of cellular activities and physicochemical change; such capability could lead to new lab-on-a-chip pharmacological platforms[9,10] and hybrid 3D electronics–tissue materials for synthetic biology[11,12].

Recently, there have been several reports describing the coupling of electronics and tissues using flexible and/or stretchable planar devices[13–17] that conform to natural tissue surfaces. These planar devices have been used to probe electrical activities near surfaces of the heart[13–15], brain[16] and skin[17]. So far, seamless 3D integration of electronics with biomaterials and synthetic tissues has not been achieved. Key points that must be addressed to achieve this goal include: the electronic structures must be macroporous, not planar, to enable 3D interpenetration with biomaterials; the electronic network should have nanometre to micrometre scale features comparable to biomaterial scaffolds; and the electronic network must have 3D interconnectivity and mechanical properties similar to biomaterials.

Here we introduce a conceptually new approach that meets this challenge by integrating nanoelectronics throughout biomaterials and synthetic tissues in three dimensions using macroporous nanoelectronic scaffolds. We use silicon nanowire field-effect transistor (FET)-based nanoelectronic biomaterials, given their capability for recording both extracellular and intracellular signals with subcellular resolution[18–21]. FET detectors respond to variations in potential at the surface of the transistor channel region, and they are typically called active detectors[21]. Metal–electrode[22,23]- or carbon nanotube/nanofibre[24,25]-based passive detectors are not considered in our work because impedance limitations (that is, signal/noise and temporal resolution degrade as the area of the metal or carbon electrodes is decreased) make it difficult to reduce the size of individual electrodes to the subcellular level[21–23], a size regime necessary to achieve a non-invasive 3D interface of electronics with cells in tissue.

Our approach (Fig. 1) involved stepwise incorporation of biomimetic and biological elements into nanoelectronic networks across nanometre to centimetre size scales. First, chemically synthesized kinked[18] or uniform silicon nanowires were deposited either randomly or in regular patterns for single-nanowire FETs—the nanoelectronic sensor elements of the hybrid biomaterials (step A, Fig. 1). Second, individual nanowire FET devices were lithographically patterned and integrated into free-standing macroporous scaffolds (step B, Fig. 1), the nanoES. The nanoES were designed to mimic ECM structures, and specifically, to be 3D, to have nanometre to micrometre features with high (>99%) porosity

[1]Department of Chemistry and Chemical Biology, Harvard University, Cambridge, Massachusetts 02138, USA, [2]Department of Anesthesiology, Division of Critical Care Medicine, Children's Hospital Boston, Harvard Medical School, Boston, Massachusetts 02115, USA, [3]David H. Koch Institute for Integrative Cancer Research, Massachusetts Institute of Technology, Cambridge, Massachusetts 02139, USA, [4]Department of Chemical Engineering, Massachusetts Institute of Technology, Cambridge, Massachusetts 02139, USA, [5]School of Engineering and Applied Sciences, Harvard University, Cambridge, Massachusetts 02138, USA. †These authors contributed equally to this work. *e-mail: Daniel.Kohane@childrens.harvard.edu; cml@cmliris.harvard.edu.

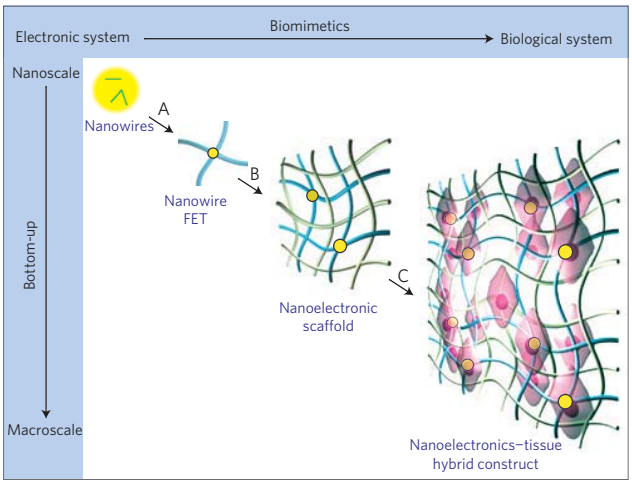

Figure 1 | Integrating nanoelectronics with cells and tissue. Conventional bulk electronics are distinct from biological systems in composition, structural hierarchy, mechanics and function. Their electrical coupling at the tissue/organ level is usually limited to the tissue surface, where only boundary or global information can be gleaned unless invasive approaches are used. We have introduced a new concept by creating an integrated system from discrete electronic and biological building blocks (for example, semiconductor nanowires, molecular precursors of polymers and single cells). Three biomimetic and bottom-up steps have been designed: step A, patterning, metallization and epoxy passivation for single-nanowire FETs; step B, forming 3D nanowire FET matrices (nanoelectric scaffolds) by self- or manual organization and hybridization with traditional ECMs; step C, incorporation of cells and growth of synthetic tissue through biological processes. Yellow dots: nanowire components; blue ribbons: metal and epoxy interconnects; green ribbons: traditional ECMs; pink: cells.

and to be highly flexible and biocompatible. NanoES were then combined with synthetic or natural macroporous ECMs providing ECMs with electrical sensory function and nanoES with biochemical environments suitable for tissue culture. Finally, cells were cultured within the nanoES (step C, Fig. 1) to yield 3D hybrid nanoelectronics–tissue constructs. The emphasis on a nanoscale and biomimetic bottom-up pathway allows minimally invasive integration of electronic devices with cells and ECM components at the subcellular level in three dimensions. The nanoES are distinct from conventional 2D multi-electrode arrays[23], carbon nanotube/nanofibre arrays[24,25], implantable micro-electrodes[23] and flexible/stretchable electrodes[13–17] in that the sensors are nanoscale semiconductors, and critically, that the sensor network is flexible, macroporous and 3D. As a result, nanoES are suitable for 3D cell cultures that are known to resemble the structure, function or physiology of living tissues.

We have designed two nanoES (Fig. 2a) that are free-standing, flexible and contain similar components. Both were fabricated on sacrificial layers, which were subsequently removed, yielding free-standing nanoES (Methods and Supplementary Figs S1 and S2). In brief, a layer of negative resist (SU-8) was coated on a nickel sacrificial layer, a solution with kinked or straight nanowires was deposited onto the SU-8 layer and allowed to evaporate, and then SU-8 was patterned by lithography to immobilize nanowires and to provide the basic framework for nanoES. Extra nanowires were washed away during the development process of the SU-8 structure. Metal contacts were patterned by lithography and deposition. Finally, a layer of SU-8 was deposited and lithographically defined as the upper passivation layer on the interconnects.

Reticular nanoES were made by electron beam lithography (EBL). Self-organization (that is, folding according to the predefined layout of bending elements) created a random or regular network of 3D features that mimic the size scale and morphology of submicron ECM features, such as the fibrous meshwork of brain ECM (ref. 26). Open mesh nanoES were made by photolithography with a regular structure, similar to the ECM of the ventricular myocardium[27,28]. 3D scaffolds were then realized in a straightforward manner by directed mesh manipulation. The planar design and initial fabrication of these 3D nanoES use existing capabilities developed for conventional planar nanoelectronics, and could enable integration of additional device components (for example, memories and logic gates)[29,30] and substantial increases in device number and overall scaffold size.

The 2D structure of the reticular scaffold was designed so that metal interconnects were stressed[18,31]. Removal of the sacrificial layer prompted self-organization into three dimensions. Reconstructed 3D confocal fluorescence images of typical reticular scaffolds viewed along the y and x axes (Fig. 2bI and II respectively) showed that the framework was 3D with a highly curvilinear and interconnected structure. The porosity (calculated from the initial planar device design and the final 3D construct volume) was >99.8%, comparable to that of hydrogel biomaterials[6–8]. Nanowire FET devices (Fig. 2bII) within the scaffold spanned separations of 7.3–324 μm in three dimensions (Supplementary Fig. S3), and the reticular scaffold heights were less than ~300 μm for our present fabrication conditions. Devices can be made closer together (for example, < 0.5 μm) by depositing nanowires more densely on the substrate[30] to improve the spatial resolution of nanoelectronic sensors; the span of device separations and scaffold heights can be increased substantially using larger field lithography (see below).

Scanning electron microscopy (SEM) of the reticular nanoES (Fig. 2c) revealed kinked nanowires (about 80 nm diameter), and metallic interconnects (about 0.7 μm width) contained within the SU-8 backbone (about 1 μm width). The feature sizes are comparable to those of synthetic and natural ECMs (refs 3, 6), and are several orders of magnitude smaller than those for electronic structures[23] penetrating tissue in three dimensions. The performance of devices was evaluated through water-gate measurements for the nanowire FET elements in the 3D scaffolds in aqueous medium (Supplementary Information). The results show device yields (~80%), conductances (1.52 ± 0.61 μS; mean ± s.d.) and sensitivities (8.07 ± 2.92 μS V^{-1}) comparable to measurements from planar devices using similar nanowires[18].

3D mesh nanoES were realized by folding and rolling free-standing device arrays. Mesh structures (Fig. 2aII) were fabricated such that the nanoES maintained an approximately planar configuration following relief from the substrate. A typical 3.5 cm × 1.5 cm × ~2 μm mesh nanoES, was approximately planar with 60 nanowire FET devices in a regular array with a 2D open porosity of 75% (Fig. 2d). This mesh porosity is comparable to that of a honeycomb-like synthetic ECM engineered for cardiac tissue culture[28]. In addition, the nanowires (Fig. 2d1), metal interconnects (Fig. 2d2) and SU-8 structural elements (Fig. 2d3) had an areal mass density of <60 μg cm^{-2}, the lowest value reported so far for flexible electronics, which reflects our macroporous architecture. The mesh nanoES was flexible and can be manually rolled into tubular constructs with inner diameters at least as small as 1.5 mm (Fig. 2e), and folded. Macroporous structures of the open mesh nanoES were formed either by loosely stacking adjacent mesh layers (Fig. 2f) or by shaping it with other biomaterials. These capabilities were consistent with the estimated ultralow effective bending stiffness (Supplementary Information), which was tuned between 0.006 and 1.3 nN m for this mesh and is comparable to recent planar epidermal electronics[17].

The electrical transport characteristics of the mesh nanoES were evaluated in phosphate buffered saline. The typical device yield is 90–97%, with average device conductance ~3 μS and sensitivity

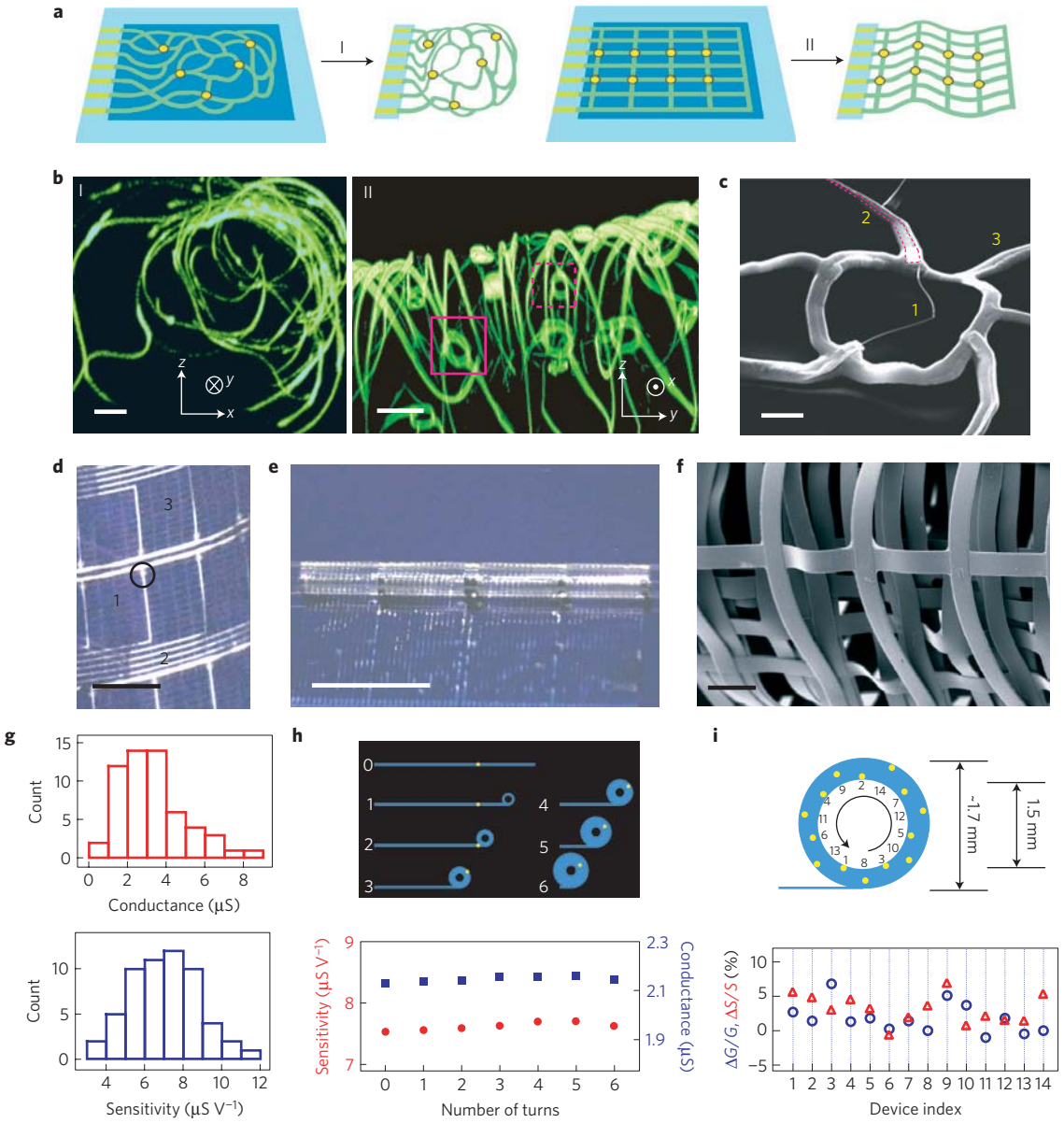

Figure 2 | Macroporous and flexible nanowire nanoES. a, Device fabrication schematics. (I) Reticular nanowire FET devices. (II) Mesh nanowire FET devices. Light blue: silicon oxide substrates; blue: nickel sacrificial layers; green: nanoES; yellow dots: individual nanowire FETs. **b**, 3D reconstructed confocal fluorescence micrographs of reticular nanoES viewed along the *y* (I) and *x* (II) axes. The scaffold was labelled with rhodamine 6G. The overall size of the structure, *x*–*y*–*z* = 300–400–200 μm. Solid and dashed open magenta squares indicate two nanowire FET devices located on different planes along the *x* axis. Scale bars, 20 μm. **c**, SEM image of a single-kinked-nanowire FET within a reticular scaffold, showing (1) the kinked nanowire, (2) metallic interconnects (dashed magenta lines) and (3) the SU-8 backbone. Scale bar, 2 μm. **d**, Photograph of a mesh device, showing (1) nanowires, (2) metal interconnects and (3) SU-8 structural elements. The circle indicates the position of a single-nanowire FET. Scale bar, 2 mm. **e**, Photograph of a partially rolled-up mesh device. Scale bar, 5 mm. **f**, SEM image of a loosely packed mesh nanoES, showing the macroporous structure. Scale bar, 100 μm. **g**, Histograms of nanowire FET conductance and sensitivity in one typical mesh nanoES. The conductance and sensitivity were measured in the water-gate configuration without rolling. The device yield for this mesh nanoES is 95%. **h**, Water-gate sensitivity and conductance of a nanowire FET in a mesh device during the rolling process. Upper panel, schematic of the nanowire FET position (yellow dot) during the rolling process; 0–6 denote the number of turns. **i**, Relative change in conductance and sensitivity of 14 nanowire FETs evenly distributed throughout a fully rolled-up mesh device. Upper panel, schematic of the nanowire FET position (yellow dots). In **h**,**i** the thicknesses of the tubular structures have been exaggerated for schematic clarity.

~7 μS V^{-1} (Fig. 2g). Representative conductance (G) data (Fig. 2h) from a single-nanowire FET (Fig. 2h, yellow dots, upper panel) during the rolling process showed a <0.17 μS conductance change (ΔG) or <2.3% total change for 6 revolutions. Device sensitivity (S) remained stable with a maximum change (ΔS) of 0.031 μS V^{-1}, or 1.5% variation. The stable performance during rolling can be explained by the low estimated strains of metal (<0.005%) and SU-8 (<0.27%) in this tubular construct (Supplementary Information), and showed that the properties were approximately independent of location. Furthermore, 14 devices evenly distributed on six layers of a rolled-up scaffold (Fig. 2i) showed maximum $\Delta G = 6.8\%$ and $\Delta S = 6.9\%$ versus the unrolled state, demonstrating device robustness. Repetitive rolling and relaxation to the flat state did not degrade the nanowire FET performance. These findings suggest the potential for reliable sensing/recording of dynamic and deformable systems.

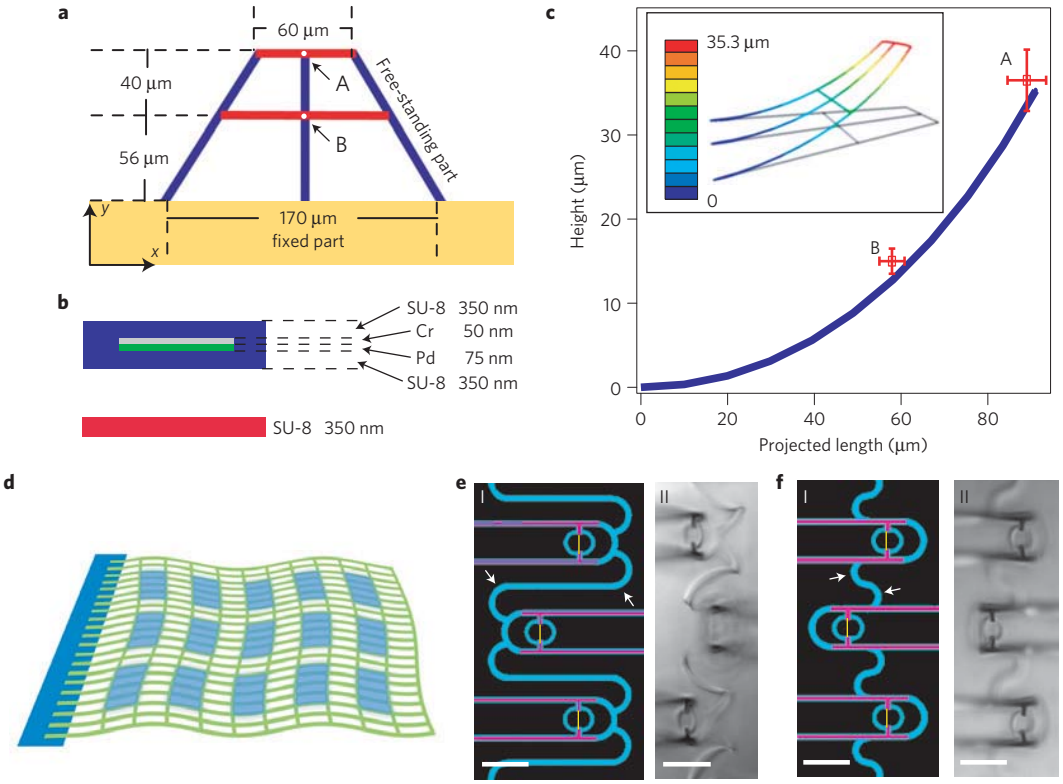

Figure 3 | Geometry control by design in nanoES. a,**b**, Basic design and structural subunit for simulation. **a**, Top-down view of the entire subunit. Blue ribbons are stressed metal lines with SU-8 passivation. Red lines are single SU-8 ribbons without residual stress. **b**, Cross-sectional views of those two key structural elements used for simulation. **c**, Plot of projected (on the *x*–*y* plane) length versus height (in the *z* direction) for the vertical blue ribbon in **a** as determined from the simulation. Open red squares with error bars are experimental data (means ±s.d.) recorded in air for point A and B in **a**. The simulation of the bending of the subunit model for the reticular structure was carried out using the commercial finite element software ABAQUS. The inset shows a 3D view of the simulated structure, and the scale bar shows different heights in the *z* direction. **d**, Schematic showing the integration of periodic reticular-device domains (light blue) into a flexible mesh (green). In individual reticular domains, the 3D device positions relative to the global flexible mesh can be controlled by their geometry designs (**a**–**c**). **e**,**f**, Design patterns (I) and experimental data (II) for two reticular units. SU-8, metal and nanowires are shown in blue, pink and yellow in **e**. Changing the structure of the connecting feature (white arrows) between adjacent device units during pattern design (I) yields controlled variations in the 3D positioning of the nanowire FETs, which can be further tuned by the stress in the metal connections. In these experiments, the device positions are 40 μm (**e**II) and 23 μm (**f**II) above the mesh plane. Scale bars in **e**,**f**, 20 μm.

We have carried out simulations of a subunit of the self-organizing reticular structure (Fig. 3a–c). Measurements of bending for the corresponding experimental structures (Fig. 3c, open red squares) are consistent with the simulation (Fig. 3c). Additionally, changes in structural parameters (for example, the total length of the subunit and thicknesses of SU-8 or metals) yield predictable changes in the bending angle of the subunit (Supplementary Fig. S4). In this way, ordered 3D nanowire FET arrays can be designed and fabricated using reticular- or mesh-like structures that incorporate multi-layer metal interconnects with built-in stress to self-organize (roll-up) the scaffold (Supplementary Fig. S4). Finally, we have designed reticular domains in mesh-like structures (Fig. 3d). Images of reticular domains (Fig. 3e,f) show that regular nanowire FET devices with distinct device positions can be realized by varying the structural parameters of individual elements. Overall, this approach yields hierarchical 3D nanoES with submicrometre to micrometre scale control in reticular domains and millimetre to centimetre scale in the mesh matrix by folding or rolling as shown above (Fig. 2).

The reticular and mesh nanoES were also merged with conventional macroporous biomaterials. Specifically, gel casting, lyophilization and electrospinning were used to deposit and construct macroporous collagen (Fig. 4a), alginate (Fig. 4b) and poly(lactic-co-glycolic acid) (PLGA; Fig. 4c), respectively, around nanoES. A confocal fluorescence micrograph of a hybrid reticular nanoES/collagen scaffold (Fig. 4a) shows clearly that the collagen nanofibres (green) are fully entangled with the nanoES, with no evidence of phase separation. SEM images of the open mesh nanoES/alginate hybrid scaffold produced by lyophilization (Fig. 4b) show that the flexible nanoES mesh is intimately anchored to the alginate framework, which has a similar pore structure as the pure alginate scaffold prepared under similar conditions. Finally, optical micrographs of a multilayered mesh nanoES/PLGA scaffold (Fig. 4c), which was prepared by electrospinning PLGA fibres on both sides of the nanoES and subsequent folding of the hybrid structure, highlight the intimate contact between nanoES mesh and PLGA fibres. The hybrid nanoES/biomaterial 3D scaffolds retain the original nanowire FET device characteristics. For example, measurements in 1 × phosphate buffered saline solution showed that $\Delta G/G$ and $\Delta S/S$ were less than ±9% for the mesh nanoES/PLGA composite versus bare nanoES. Hybrid nanoES were stable under cell culture conditions. For example, nanowire FET devices in the hybrid reticular nanoES/Matrigel scaffold in neuron culture media (Fig. 4d) had $\Delta S/S < \pm 11\%$ over a nine-week period, suggesting a capability for long-term culture and monitoring with the nanoES. These results show that nanoES can be combined with conventional biomaterials to produce hybrid scaffolds that now provide nanoscale electrical sensory components distributed in three dimensions.

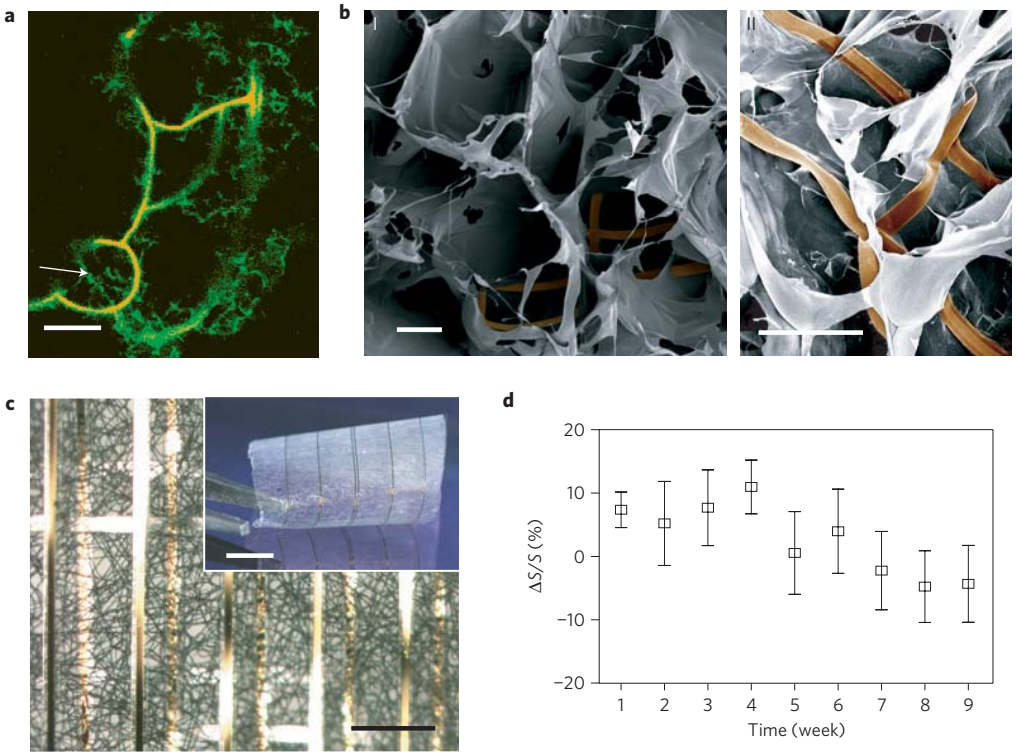

Figure 4 | Hybrid macroporous nanoelectronic scaffolds. a, Confocal fluorescence micrograph of a hybrid reticular nanoES/collagen matrix. Green (fluorescein isothiocyanate): collagen type-I; orange (rhodamine 6G): epoxy ribbons. The white arrow marks the position of the nanowire. Scale bar, 10 μm. **b**, SEM images of a mesh nanoES/alginate scaffold, top (I) and side (II) views. The epoxy ribbons from nanoES are false-coloured in brown for clarity. Scale bars, 200 μm (I) and 100 μm (II). **c**, A bright-field optical micrograph of the folded scaffold, showing multilayered structures of PLGA and nanoelectronic interconnects. The inset shows a photograph of the hybrid sheet before folding. A sheet of PLGA fibres with diameters of ~1–3 μm was deposited on both sides of the device. No damage or reduction of device yield was observed following this deposition. Scale bars, 200 μm and 5 mm (inset). **d**, Relative changes in nanowire FET sensitivity over time in culture (37 °C; 5% CO_2, supplemented neurobasal medium). $n = 5$; data are means ±s.d.

The hybrid nanoES were evaluated in 3D culture[32,33] for several cell types. Embryonic rat hippocampal neurons were cultured in the reticular nanoES/Matrigel for 7–21 days (Supplementary Fig. S5). Reconstructed 3D confocal micrographs from a two-week culture (Fig. 5a,b and Supplementary Fig. S6) showed neurons with a high density of spatially interconnected neurites that penetrated the reticular nanoES (Fig. 5a), often passing through the ring structures supporting individual nanowire FETs (Fig. 5b and Supplementary Fig. S6). Notably, the widths of the scaffold elements (passivated metal interconnects and structural ribbons) were similar to those of the neurite projections, demonstrating the combination of electronics with biological systems at an unprecedented similarity in scale. 3D nanoelectronic cardiac culture was achieved from hybrid mesh nanoES/PLGA scaffolds (Supplementary Figs S7–S9). Confocal fluorescence microscopy of a cardiac 3D culture (Fig. 5c) revealed a high density of cardiomyocytes in close contact with nanoES components. Epifluorescence micrographs of cardiac cells on the surface of the nanoES cardiac patch showed striations characteristic of cardiac tissue[28,32] (Fig. 5d and Supplementary Figs S8 and S9). In addition, the *in vitro* cytotoxicity of nanoES in 3D neural and cardiac culture was evaluated (Fig. 5e,f). Differences between hippocampal neurons in reticular nanoES/Matrigel versus Matrigel over 21 days, assessed with a standard LIVE/DEAD cell assay[33] (Fig. 5e), and between cardiac cells in hybrid mesh nanoES/Matrigel/PLGA and Matrigel/PLGA from 2 to 12 days, measured with a metabolic activity assay (Fig. 5f), were minimal. These studies show that on the 2–3 week timescale, the nanoES component of the scaffolds has little effect on the cell viability, and thus can be exploited for a number of *in vitro* studies, including drug screening assays with these synthetic neural and cardiac tissues. Extended studies will be needed to evaluate the nanoES for longer-term implants, although the main component of nanoES, SU-8, has demonstrated long-term chronic biocompatibility suitable for *in vivo* recording[34,35].

The monitoring capabilities of the nanoES were first demonstrated in a 3D cardiomyocyte mesh construct (Fig. 5g). The output recorded from a single-nanowire FET (Fig. 5g) ~200 μm below the construct surface showed regularly spaced spikes with a frequency of ~1 Hz, a calibrated potential change of ~2–3 mV, a signal/noise ≥3 and a ~2 ms width. The peak amplitude, shape and width are consistent with extracellular recordings from cardiomyocytes[20]. The potential of the nanoES-based 3D cardiac culture to monitor appropriate pharmacological response was investigated by dosing the 3D cardiomyocyte mesh construct with noradrenaline (also known as norepinephrine), a drug that stimulates cardiac contraction through β_1-adrenergic receptors[36]. Measurements from the same nanowire FET device showed a twofold increase in the contraction frequency following drug application. Interestingly, recordings from two nanowire FETs from the cardiac patch on noradrenaline application showed submillisecond and millisecond level, heterogeneous cellular responses to the drug (Supplementary Fig. S10). Additionally, multiplexing measurements made with a reticular nanoES/neural construct (Supplementary Fig. S11) showed that the 3D response of glutamate activation could be monitored. Together these experiments suggest nanoES constructs can monitor *in vitro* the response to drugs from 3D tissue models, and thus have potential as a platform for *in vitro* pharmacological studies[9,10]. Last, simultaneous recordings from four nanowire FETs with separations up to 6.8 mm in a nanoES/cardiac construct (Fig. 5h) demonstrated multiplexed sensing

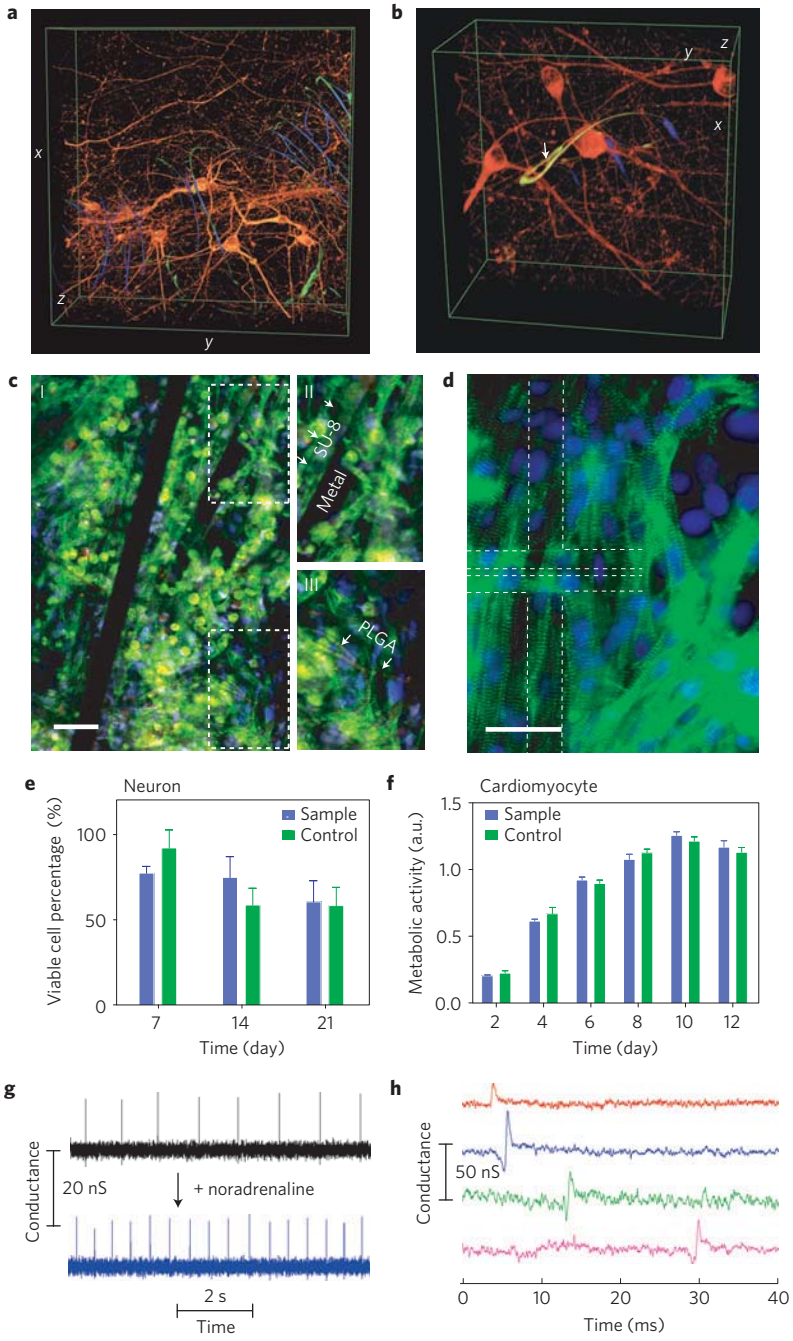

Figure 5 | 3D cell culture and electrical sensing in nanoES. a,**b**, 3D reconstructed confocal images of rat hippocampal neurons after a two-week culture in Matrigel on reticular nanoES. Red (Alexa Fluor 546): neuronal β-tubulin; yellow (rhodamine 6G): epoxy ribbons. The metal interconnects are false-coloured in blue, and are imaged in the reflected light mode. The white arrow highlights a neurite passing through a ring-like structure supporting a nanowire FET. Dimensions in **a**, *x*: 317 μm; *y*: 317 μm; *z*: 100 μm; in **b**, *x*: 127 μm; *y*: 127 μm; *z*: 68 μm. **c**, Confocal fluorescence micrographs of a synthetic cardiac patch. (II and III), Zoomed-in view of the upper and lower dashed regions in I, showing metal interconnects, the SU-8 scaffold (arrows in II) and electrospun PLGA fibres (arrows in III). Scale bar, 40 μm. **d**, Epifluorescence micrograph of the surface of the cardiac patch. Green (Alexa Fluor 488): α-actin; blue (Hoechst 34580): cell nuclei. The position of the source–drain electrodes is outlined with dashed lines. Scale bar, 40 μm. **e**, Percentage of viable hippocampal neurons cultured in nanoES/Matrigel versus Matrigel. Cell viability was evaluated with a LIVE/DEAD cytotoxicity assay. Cells were counted from 3D reconstructed confocal fluorescence micrographs. $n = 6$; data are means ±s.d. Differences between groups were very small although statistically significant ($p < 0.05$). **f**, Metabolic activity of cardiomyocytes evaluated using the MTS assay. $n = 6$; data are means ±s.d. Differences between groups were very small although statistically significant ($p < 0.05$). **g**, Conductance versus time traces recorded from a single-nanowire FET before (black) and after (blue) applying noradrenaline. **h**, Multiplex electrical recording of extracellular field potentials from four nanowire FETs in a mesh nanoES. Data are conductance versus time traces of a single spike recorded at each nanowire FET.

of a coherently beating cardiac patch, with submillisecond time resolution. Our current device design yields relatively sparse device distribution with 60 devices over an area of about $3.5 \times 1.5\,cm^2$. Increases in nanowire FET density, the use of cross-bar circuits and implementing multiplexing/demultiplexing for addressing[30] could allow the nanoES scaffolds to map cardiac and other synthetic

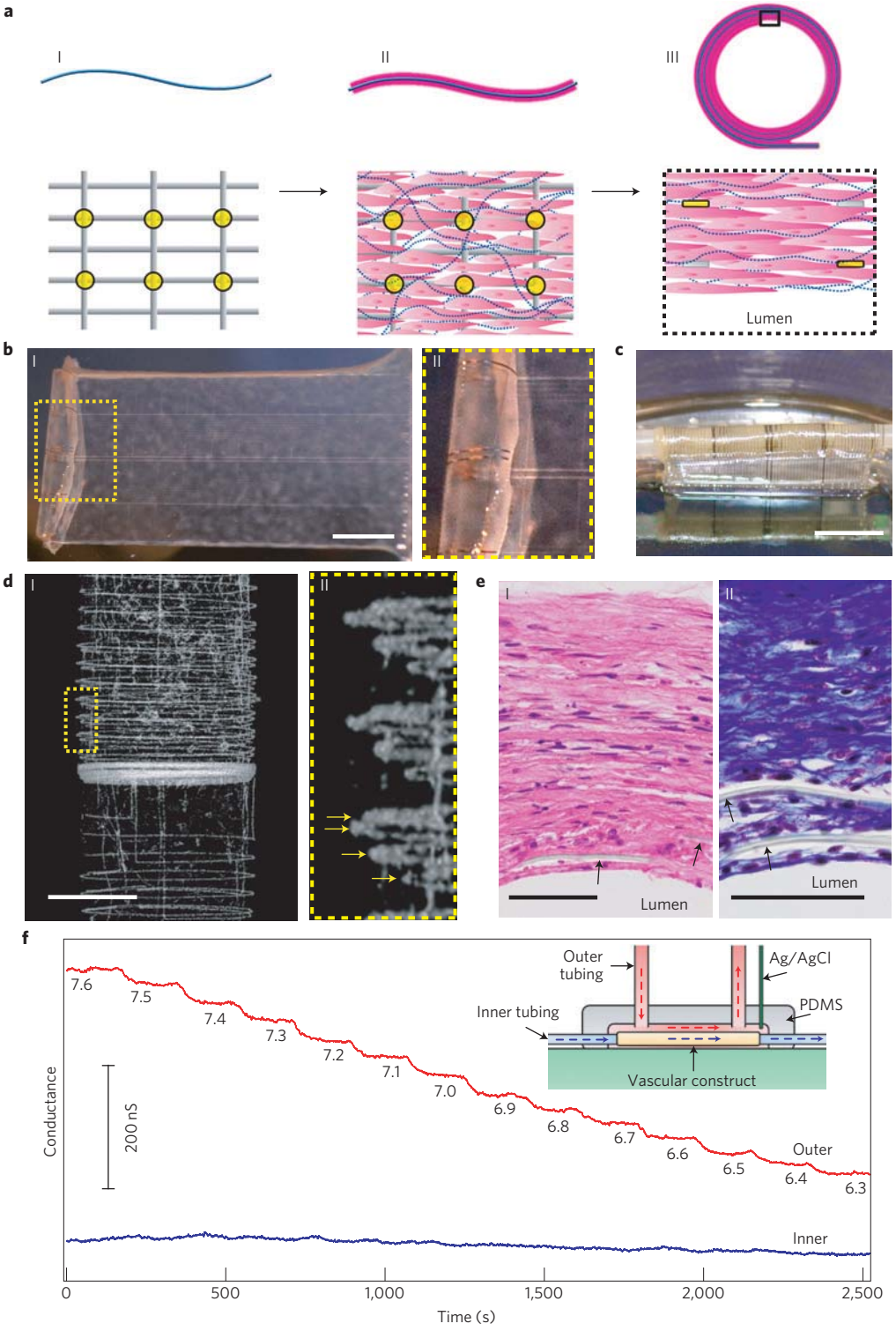

Figure 6 | Synthetic vascular construct enabled for sensing. a, Schematic of the synthesis of smooth muscle nanoES. The upper panels are side views, and the lower ones are either top views (I and II) or a zoom-in view (III). Grey: mesh nanoES; blue fibres: collagenous matrix secreted by HASMCs; yellow dots: nanowire FETs; pink: HASMCs. **b**, (I) Photograph of a single HASMC sheet cultured with sodium L-ascorbate on a nanoES. (II) Zoomed-in view of the dashed area in I, showing metallic interconnects macroscopically integrated with cellular sheet. Scale bar, 5 mm. **c**, Photograph of the vascular construct after rolling into a tube and maturation in a culture chamber for three weeks. Scale bar, 5 mm. **d** (I) Micro-computed tomograph of a tubular construct segment. (II) Zoomed-in view of the area outlined in I. The arrows mark the individual nanowire FET-containing layers of the rolled construct. Scale bar, 1 mm. **e**, Haematoxylin–Eosin- (I) and Masson-Trichrome- (II; collagen is blue) stained sections (~6 μm thick) cut perpendicular to the tube axis; lumen regions are labelled. The arrows mark the positions of SU-8 ribbons of the nanoES. Scale bars, 50 μm. **f**, Changes in conductance over time for two nanowire FET devices located in the outermost (red) and innermost (blue) layers. The inset shows a schematic of the experimental set-up. Outer tubing delivered bathing solutions with varying pH (red dashed lines and arrows); inner tubing delivered solutions with fixed pH (blue dashed lines and arrows).

tissue electrical activities over the entire constructs at high density in three dimensions.

We have also extended our approach towards the development of artificial tissue with embedded nanoelectronic sensory capabilities. Specifically, vascular nanoES constructs were prepared by processes analogous to those used for tissue-engineered autologous blood vessels[37,38] except for the addition of the nanoES (Fig. 6a and Supplementary Fig. S12). Human aortic smooth muscle cells (HASMCs) were cultured on 2D mesh nanoES with sodium ascorbate to promote the deposition of natural ECM. The hybrid nanoES/HASMC sheets (Fig. 6b) were rolled into multi-layer 3D tubular structures and matured (Supplementary Information) without macroscopic delamination or desquamation (Fig. 6c), and analyses showed that the cells expressed smooth muscle α-actin (Supplementary Fig. S13), the key contractile protein in smooth muscle[37].

The distribution of nanoES in the tubular construct was visualized by micro-computed tomography (μCT). A projection of the reconstructed 3D μCT data (Fig. 6d) revealed regularly spaced metal interconnects with at least four revolutions (arrows, Fig. 6dII), consistent with the nanowire FET mesh and tissue rolling. Analyses of haemotoxylin–Eosin- and Masson-trichrome-stained sections (Fig. 6e) revealed smooth muscle tissue ∼200 μm thick, with elongated cells and collagenous nanofibres, and embedded SU-8 ribbons from the nanoES (Fig. 6e). These findings confirm the 3D integration of nanowire FET nanoelectronics with healthy smooth muscle.

The potential of this vascular construct to function as a biomedical device was demonstrated by 3D pH sensing (Fig. 6f, inset). As the extravascular pH was varied stepwise with luminal pH fixed, simultaneous recordings from p-type nanowire FETs in the outermost layer showed stepwise conductance decreases with a sensitivity of ∼32 mV per unit of pH. nanowire FETs in the innermost layer (closest to luminal) showed minor baseline fluctuations. This ability to resolve extravascular pH changes makes possible the detection of inflammation, ischaemia, tumour micro-environments or other forms of metabolic acidosis due to overproduction of organic acids or impaired renal acidification[39,40], although we stress that the implantation of these nanoES-based vascular and other nanoES-embedded constructs for *in vivo* studies will require substantial future work.

The nanoES concept and implementations described here represent a new direction in merging nanoelectronics with biological systems because we have demonstrated a 3D macroporous material/device platform that is distinct from either engineered tissue[6,41] or flexible electronics[13–17,42–44]. Looking forward, there are several areas to develop. Cell interactions with nanoES could be tuned by modification of the nanoES with growth determinants[6,32]. In addition, the elements in the nanoES could be expanded to incorporate nanoscale stimulators and stretchable designs to provide electrical and mechanical stimulation to enhance cell culture.

Methods

Kinked and uniform silicon nanowires were synthesized by the nanocluster-catalysed methods described previously[18]. Devices were fabricated on silicon substrates (Nova Electronic Materials, n-type 0.005 V cm) with 600 nm SiO_2 or 100 nm SiO_2/200 nm Si_3N_4 at the surface. EBL and photolithography on nickel relief layers were used to define the metal contacts to the nanowires and the principal features of the scaffolds. The key steps used in the fabrication of the reticular nanoES were as follows. First, 100 nm nickel metal was patterned and deposited, and served as the relief layer for the free-standing scaffolds. Next, a 300–500 nm layer of SU-8 photoresist (2000.5, MicroChem, Newton) was deposited over the entire chip (Supplementary Fig. S1c) followed by pre-baking at 65 °C and 95 °C for 2 and 4 min, respectively; then an isopropanol solution of n^+–n–n^+ kinked nanowires was deposited onto the SU-8 layer. After identifying nanowire positions by optical imaging (Olympus BX51) and designing the interconnect and SU-8 patterns in IGOR Pro (WaveMetrics) and DesignCAD, EBL was used to pattern the overall SU-8 scaffold structure around chosen nanowires, which was post-baked (65 °C and 95 °C for 2 and 4 min, respectively) and cured (180 °C, 20 min) to yield the flexible structural support for metal interconnects. The silicon substrate was then coated with a methyl methacrylate and poly(methyl methacrylate) double-layer resist, the resist was patterned over the chosen SU-8 ribbons and then non-symmetrical Cr/Pd/Cr (1.5/50–80/50–80 nm) metals were sequentially deposited followed by metal lift-off in acetone to form the nanowire interconnects. The non-symmetrical Cr/Pd/Cr layer structure yields a built-in stress, which drove 3D self-organization when the structure was relieved from the substrate. The silicon substrate was then coated with a uniform 300–400 nm layer of SU-8, and EBL of SU-8 followed by curing (180 °C, 20 min) was used to define the SU-8 passivation layer over the deposited metal interconnects. The reticular nanoES, including the interconnected kinked nanowire FET devices, were released from the substrate by etching of the nickel layer (Nickel Etchant TFB, Transene Company, Danvers) for 60–120 min at 25 °C. Last, the free-standing nanoES were dried using a critical point dryer (Autosamdri 815 Series A, Tousimis) and stored in the dry state before use in tissue culture. Each EBL step will take 10 min–2 h depending on the writing speed and area, feature size and complexity, and electron beam dosage (for example, the typical area dosages for SU-8 and poly(methyl methacrylate) EBL are 3–8 μC cm^{-2} and 500–1,000 μC cm^{-2} at 25 kV, respectively). The entire fabrication took 2–5 days depending on the duration of the individual steps. A similar approach was used in the fabrication of the mesh nanoES (Supplementary Information), except that p-type nanowires and photolithography were used and the entire process took 2–3 days.

NanoES/collagen(Matrigel) hybrid matrices were made by casting 50 ∼ 2,000 μl collagen or Matrigel solution onto the edge of (reticular nanoES) or directly above (mesh nanoES) the nanoES scaffolds, and at ∼4 °C. The solutions were allowed to form gels around nanoES under conditions of 37 °C and 5% CO_2 for at least 20 min. The 3D nanoES/alginate scaffolds were prepared from pharmaceutical-grade alginate (Protanal LF5/60, FMC Biopolymers) by calcium gluconate crosslinking and subsequent lyophilization to produce a sponge-like scaffold (5–15 mm × 2–10 mm, $d \times h$). To prepare NanoES/PLGA hybrid scaffolds, a sheet of PLGA fibres with diameters of ∼1–3 μm was deposited on both sides of the mesh nanoES. The hybrid scaffold can be folded to increase the thickness.

Embryonic Sprague/Dawley rat hippocampal cells, neonatal Sprague/Dawley rat cardiomycytes and HASMCs were cultured in nanoES using established protocols (Supplementary Information). Optical micrographs of immunohistochemically and histologically stained samples were recorded using either Olympus Fluoview FV1000 or Olympus FSX100 systems. The structures of nanoES were characterized with Zeiss Ultra55/Supra55VP field-emission SEMs or the HMXST micro-computed tomography X-ray imaging system (model: HMXST225, X-Tek). The *in vitro* cytotoxicity of nanoES was evaluated using the standard LIVE/DEAD Viability/Cytotoxicity Kit (Molecular Probes, Invitrogen) and the CellTiter 96 AQueous One Solution Cell Proliferation Assay (Promega Corporation). Cardiomyocyte recordings were carried out in Tyrode solution with a 100 mV d.c. source for the nanowire FETs. The current was amplified with a multi-channel preamplifier, filtered with a 3 kHz low-pass filter (CyberAmp 380) and digitized at a 50 kHz sampling rate[18–20] (Axon Digi1440A). In extravascular pH sensing experiments, a single polydimethylsiloxane microfluidic chamber was used to deliver two flows of phosphate buffer solution, where inner and outer tubings were used to deliver solutions with fixed and varied pH, respectively. The electrical measurements were conducted using a lock-in amplifier with a modulation frequency of 79 and 39 Hz, a time constant of 30 ms and an amplitude of 30 mV; the d.c. source–drain potential is zero. Ag/AgCl reference electrodes were used in all recording and sensing experiments. The calibrated potential values (in millivolts) recorded from nanowire FETs were obtained as the ratios between device conductance changes (in nanosiemens) and the sensitivities (in microsiemens per volt or nanosiemens per volt) that are determined individually in water-gate experiments.

Received 27 February 2012; accepted 19 July 2012; published online 26 August 2012

References

1. Na, K. *et al.* Directing zeolite structures into hierarchically nanoporous architectures. *Science* **333,** 328–332 (2011).
2. Schaedler, T. A. *et al.* Ultralight metallic microlattices. *Science* **334,** 962–965 (2011).
3. Place, E. S., George, J. H., Williams, C. K. & Stevens, M. M. Synthetic polymer scaffolds for tissue engineering. *Chem. Soc. Rev.* **38,** 1139–1151 (2009).
4. Wylie, R. G. *et al.* Spatially controlled simultaneous patterning of multiple growth factors in three-dimensional hydrogels. *Nature Mater.* **10,** 799–806 (2011).
5. Kloxin, A. M., Kasko, A. M., Salinas, C. N. & Anseth, K. S. Photodegradable hydrogels for dynamic tuning of physical and chemical properties. *Science* **324,** 59–63 (2009).
6. Dvir, T., Timko, B. P., Kohane, D. S. & Langer, R. Nanotechnological strategies for engineering complex tissues. *Nature Nanotech.* **6,** 13–22 (2011).
7. Kraehenbuehl, T. P., Langer, R. & Ferreira, L. Three-dimensional biomaterials for the study of human pluripotent stem cells. *Nature Methods* **8,** 731–736 (2011).

8. Hutmacher, D. W. Biomaterials offer cancer research the third dimension. *Nature Mater.* **9,** 90–93 (2010).
9. Huh, D. *et al.* Reconstituting organ-level lung functions on a chip. *Science* **328,** 1662–1668 (2010).
10. Baker, M. Tissue models: A living system on a chip. *Nature* **471,** 661–665 (2011).
11. Schwille, P. Bottom-up synthetic biology: Engineering in a Tinkerer's world. *Science* **333,** 1252–1254 (2011).
12. Ruder, W. C., Lu, T. & Collins, J. J. Synthetic biology moving into the clinic. *Science* **333,** 1248–1252 (2011).
13. Timko, B. P. *et al.* Electrical recording from hearts with flexible nanowire device arrays. *Nano Lett.* **9,** 914–918 (2009).
14. Viventi, J. *et al.* A conformal, bio-interfaced class of silicon electronics for mapping cardiac electrophysiology. *Sci. Transl. Med.* **2,** 24ra22 (2010).
15. Kim, D-H. *et al.* Materials for multifunctional balloon catheters with capabilities in cardiac electrophysiological mapping and ablation therapy. *Nature Mater.* **10,** 316–323 (2011).
16. Viventi, J. *et al.* Flexible, foldable, actively multiplexed, high-density electrode array for mapping brain activity *in vivo*. *Nature Neurosci.* **14,** 1599–1605 (2011).
17. Kim, D-H. *et al.* Epidermal electronics. *Science* **333,** 838–843 (2011).
18. Tian, B. *et al.* Three-dimensional, flexible nanoscale field-effect transistors as localized bioprobes. *Science* **329,** 831–834 (2010).
19. Qing, Q. *et al.* Nanowire transistor arrays for mapping neural circuits in acute brain slices. *Proc. Natl Acad. Sci. USA* **107,** 1882–1887 (2010).
20. Cohen-Karni, T., Timko, B. P., Weiss, L. E. & Lieber, C. M. Flexible electrical recording from cells using nanowire transistor arrays. *Proc. Natl Acad. Sci. USA* **106,** 7309–7313 (2009).
21. Timko, B. P., Cohen-Karni, T., Qing, Q., Tian, B. & Lieber, C. M. Design and implementation of functional nanoelectronic interfaces with biomolecules, cells, and tissue using nanowire device arrays. *IEEE Trans. Nanotech.* **9,** 269–280 (2010).
22. Prohaska, O. J., Olcaytug, F., Pfundner, P. & Dragaun, H. Thin-film multiple electrode probes: Possibilities and limitations. *IEEE Trans. Biomed Eng.* **33,** 223–229 (1986).
23. Nicolelis, M. A. L. (ed.) *Methods for Neural Ensemble Recordings* 2nd edn (CRC, 2008).
24. McKnight, T. E. *et al.* Resident neuroelectrochemical interfacing using carbon nanofibre arrays. *J. Phys. Chem. B* **110,** 15317–15327 (2006).
25. Yu, Z. *et al.* Vertically aligned carbon nanofibre arrays record electrophysiological signals from hippocampal slices. *Nano Lett.* **7,** 2188–2195 (2007).
26. Dequach, J. A., Yuan, S. H., Goldstein, L. S. & Christman, K. L. Decellularized porcine brain matrix for cell culture and tissue engineering scaffolds. *Tissue Eng. A* **17,** 2583–2592 (2011).
27. Hanley, P. J., Young, A. A., LeGrice, I. J., Edgar, S. G. & Loiselle, D. S. Three dimensional configuration of perimysial collagen fibres in rat cardiac muscle at resting and extended sarcomere lengths. *J. Physiol.* **517,** 831–837 (1999).
28. Engelmayr, G. C. Jr *et al.* Accordion-like honeycombs for tissue engineering of cardiac anisotropy. *Nature Mater.* **7,** 1003–1010 (2008).
29. Lu, W. & Lieber, C. M. Nanoelectronics from the bottom up. *Nature Mater.* **6,** 841–850 (2007).
30. Yan, H. *et al.* Programmable nanowire circuits for nanoprocessor. *Nature* **470,** 240–244 (2011).
31. Wang, M. F., Maleki, T. & Ziaie, B. Enhanced three-dimensional folding of silicon microstructures via thermal shrinkage of a composite organic/inorganic bilayer. *IEEE/ASME J. Microelectromech. Syst.* **17,** 882–889 (2008).
32. Sapir, Y., Kryukov, O. & Cohen, S. Integration of multiple cell-matrix interactions into alginate scaffolds for promoting cardiac tissue regeneration. *Biomaterials* **32,** 1838–1847 (2011).
33. Xu, T. *et al.* Electrophysiological characterization of embryonic hippocampal neurons cultured in a 3D collagen hydrogel. *Biomaterials* **30,** 4377–4383 (2009).
34. Cho, S. H. *et al.* Biocompatible SU-8-based microprobes for recording neural spike signals from regenerated peripheral nerve fibres. *IEEE Sensors J.* **8,** 1830–1836 (2008).
35. Voskerician, G. *et al.* Biocompatibility and biofouling of MEMS drug delivery devices. *Biomaterials* **24,** 1959–1967 (2003).
36. Zipes, D. P. & Jalife, J. *Cardiac Electrophysiology: From Cell to Bedside* 5th edn (Saunders, 2009).
37. L'Heureux, N., Pâquet, S., Labbé, R., Germain, L. & Auger, F. A. A completely biological tissue-engineered human blood vessel. *FASEB J.* **12,** 47–56 (1998).
38. L'Heureux, N. *et al.* Human tissue-engineered blood vessels for adult arterial revascularization. *Nature Med.* **12,** 361–365 (2006).
39. Neri, D. & Supuran, C. T. Interfering with pH regulation in tumours as a therapeutic strategy. *Nature Rev. Drug Discov.* **10,** 767–777 (2011).
40. Kraut, J. A. & Madias, N. E. Metabolic acidosis: pathophysiology, diagnosis and management. *Nature Rev. Nephrol.* **6,** 274–285 (2010).
41. Dvir, T. *et al.* Nanowired three-dimensional cardiac patches. *Nature Nanotech.* **6,** 720–725 (2011).
42. Sekitani, T. *et al.* A rubberlike stretchable active matrix using elastic conductors. *Science* **321,** 1468–1472 (2008).
43. Mannsfeld, S. C. B. *et al.* Highly sensitive flexible pressure sensors with micro-structured rubber as the dielectric layer. *Nature Mater.* **9,** 859–864 (2010).
44. Takei, K. *et al.* Nanowire active matrix circuitry for low-voltage macro-scale artificial skin. *Nature Mater.* **9,** 821–826 (2010).

Acknowledgements

We thank F. Kosar for help on μCT imaging of synthetic tissue samples and J. L. Huang for assistance with culture chamber preparation. C.M.L. acknowledges support from a NIH Director's Pioneer Award and a McKnight Foundation Technological Innovations in Neurosciences Award. D.S.K. acknowledges a Biotechnology Research Endowment from the Department of Anesthesiology at Children's Hospital Boston and NIH grant GM073626. R.S.L. acknowledges NIH grants DE013023 and DE016516.

Author contributions

B.T., J.L., T.D., D.S.K. and C.M.L. designed the experiments. B.T. and J.L. performed experiments. T.D., J.T. and Q.Q. assisted in the initial stage of the project. L.J. and Z.S. performed calculations and simulations. B.T., J.L., D.S.K. and C.M.L. wrote the paper. All authors discussed the results and commented on the manuscript.

Additional information

Supplementary information is available in the online version of the paper. Reprints and permissions information is available online at www.nature.com/reprints. Correspondence and requests for materials should be addressed to D.S.K. or C.M.L.

Competing financial interests

The authors declare no competing financial interests.